Enforcing positiveness on estimated spectral densities

A. Stoica, R. Moses and P. Stoica

Indexing terms: Signal processing, Spectral estimation, Optimisation

Estimated spectral densities may often take on negative values in some frequency bands, and hence need be corrected to become positive for all frequencies. The Letter describes a most natural approach to enforcing the positiveness condition on an estimated spectral density, which is shown to lead to a semi-infinite optimisation problem. In the numerical example reported, the latter problem is solved by using the Matlab Optimization Toolbox.

Problem statement: Let $\{\hat{r}_k\}_{k=0}^{n}$ denote the estimated covariances of a discrete time stationary signal. The corresponding estimated

spectral density is given by

$$\hat{\phi}(\omega) = \hat{f}(e^{i\omega}) \qquad \hat{f}(z) = \sum_{k=-n}^{n} \hat{r}_{|k|} z^k \qquad (1)$$

Hereafter, ω denotes the (angular) frequency variable. As $\hat{\phi}(\omega)$ is an even periodic function of ω, with period 2π, it suffices to consider eqn. 1 for $\omega \in [0, \pi]$. Estimated spectral densities having the above form are ubiquitous in signal processing applications. They are encountered both in nonparametric applications (e.g. based on the Blackman-Tukey approach) and in parametric spectral estimation applications (e.g. by using an MA or ARMA model).

Several commonly-used methods for spectral estimation do not guarantee that $\hat{\phi}(\omega) \geq 0$ for all ω in $[0, \pi]$, and hence they may yield estimates with negative values at some frequencies. As such a situation is not acceptable for most applications, several researchers have proposed methods for enforcing the positiveness condition on an estimated $\hat{\phi}(\omega)$ (see, for example, [1–5]). Some of these methods are simple to apply, but rather ad-hoc [3–5]. Others are optimal, albeit in a limited sense, but they are somewhat intricate from an algorithmic standpoint [1, 2]. This Letter shows that a most general approach to enforcing the positiveness condition on $\hat{\phi}(\omega)$ naturally leads to a semi-infinite optimisation problem, the solution of which can be obtained for instance by using the Matlab Optimization Toolbox.

Proposed solution: Let

$$\varphi(\omega) = [1 \quad \cos\omega \ldots \cos n\omega]^T \qquad (2)$$

$$\hat{\rho} = [\hat{r}_0 \quad 2\hat{r}_1 \ldots 2\hat{r}_n]^T \qquad (3)$$

By making use of this notation, $\hat{\phi}(\omega)$ can be written as

$$\hat{\phi}(\omega) = \hat{\rho}^T \varphi(\omega) \qquad (4)$$

Whenever $\hat{\phi}(\omega)$ is not positive for all $\omega \in [0, \pi]$, a vector ρ which gives a valid spectral density

$$\phi(\omega) = \rho^T \varphi(\omega) \geq 0 \qquad \omega \in [0, \pi] \qquad (5)$$

is to be determined such that $\phi(\omega)$ is 'close to' $\hat{\phi}(\omega)$. A natural formulation of this problem is as follows:

$$\min_{\rho} \frac{1}{\pi} \int_0^{\pi} W(\omega)[\hat{\phi}(\omega) - \phi(\omega)]^2 \, d\omega$$
$$\text{subject to} \quad \phi(\omega) \geq 0 \quad \text{for} \quad \omega \in [0, \pi] \qquad (6)$$

In eqn. 6, $W(\omega)$ is a weighting function that can be used to emphasise certain frequency bands.

A straightforward calculation shows that eqn. 6 can be re-written in the following more convenient form:

$$\min_{\rho} (\hat{\rho} - \rho)^T Q (\hat{\rho} - \rho)$$
$$\text{subject to} \quad \rho^T \varphi(\omega) \geq 0 \quad \text{for} \quad \omega \in [0, \pi] \qquad (7)$$

where

$$Q = \frac{1}{\pi} \int_0^{\pi} W(\omega) \varphi(\omega) \varphi^T(\omega) \, d\omega \qquad (8)$$

For simplicity, in the following we consider the common choice $W(\omega) = 1$. For this case Q is readily derived:

$$Q = \begin{bmatrix} 1 & & & 0 \\ & 1/2 & & \\ & & \ddots & \\ 0 & & & 1/2 \end{bmatrix} \qquad (9)$$

Matrix Q above differs only slightly from the choice $Q = I$ considered in [1]. Of course, other choices of $W(\omega)$ in eqn. 8 may lead to completely different Q matrices.

Next, we note that eqn. 7 is a semi-infinite optimisation problem which can be solved by a variety of algorithms. Here we use the function 'seminf' in the Optimization Toolbox of Matlab. The initial estimate required to start seminf can be determined as follows. Let ω_1 and ω_2 be such that

$$\hat{\phi}(\omega_1) = \hat{\phi}(\omega_2) = 0 \quad \text{and} \quad \hat{\phi}(\omega) < 0 \quad \omega \in (\omega_1, \omega_2) \qquad (10)$$

(ω_1 and ω_2 can be obtained either by rooting $\hat{\phi}(z)$ or by inspection of the plot of $\hat{\phi}(\omega)$). If $\bar{\omega} = (\omega_1 + \omega_2)/2 \neq 0$ or π, then compute

$$z^n \tilde{f}(z) = [z^n \tilde{f}(z)/(z - e^{i\omega_1})(z - e^{i\omega_2})(z - e^{-i\omega_1})(z - e^{-i\omega_2})]$$
$$\times (z - e^{i\bar{\omega}})^2 (z - e^{-i\bar{\omega}})^2 \qquad (11)$$

If $\bar{\omega} = 0$ or π, then $\tilde{f}(z)$ is redefined as

$$z^n \tilde{f}(z) = [z^n \hat{f}(z)/(z - e^{i\omega_1})(z - e^{i\omega_2})](z - e^{i\bar{\omega}})^2 \qquad (12)$$

By construction, $\tilde{\phi}(\omega) \triangleq \tilde{f}(e^{i\omega})$ is non-negative for $\omega \in [\omega_1, \omega_2]$. Continuing in the above simple way, as necessary, we can obtain a corrected spectral estimate that is non-negative for all frequencies. This estimate is used as the starting point for seminf. An improved initial estimate can be obtained by optimally scaling $\tilde{f}(z)$ determined as above. The optimal scaling factor is determined by the minimisation of the criterion in eqn. 7. This amounts to solving a very simple least-squares problem, the details of which are omitted in the interest of brevity.

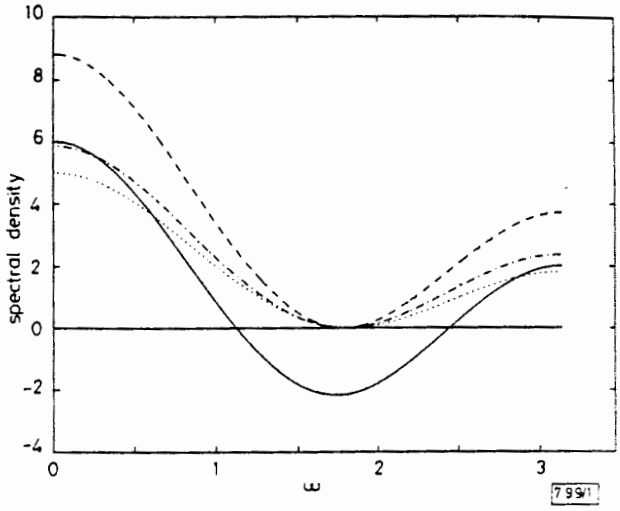

Fig. 1 Initial and corrected spectral densities

——— given $\hat{\phi}(\omega)$
– – – – initial $\tilde{\phi}(\omega)$
· · · · · optimally corrected $\phi(\omega)$
– · – · corrected $\phi(\omega)$ in [1]

Numerical example: For illustration purposes, we consider one of the examples in [1]. Let $\hat{\rho} = [1\ 2\ 3]^T$. The corresponding $\hat{\phi}(\omega)$ does not satisfy eqn. 5, as shown in Fig. 1. The correction method based on eqn. 11 yields $\tilde{\rho} = [3.270\ 2.544\ 3.000]^T$ and $\tilde{\phi}(\omega)$ exhibited in Fig. 1. The optimal correction method, which uses the function seminf (initialised by $\tilde{\rho}$) to solve the semi-infinite optimisation problem eqn. 7, gives $\rho = [1.800\ 1.600\ 1.600]^T$ and $\phi(\omega)$ shown in Fig. 1. For comparison, Fig. 1 also includes the solution derived in [1], which corresponds to using the slightly different weight $Q = I$ in eqn. 7 (the corresponding ρ is $\rho = [2.154\ 1.743\ 1.960]^T$). As expected, the corrected $\phi(\omega)$ obtained with the method of this Letter is closer to $\hat{\phi}(\omega)$ than is the corrected spectral density derived in [1]. In fact, the values of the criterion in eqn. 7 corresponding to $\tilde{\rho}$, ρ_{opt} and $\rho_{[1]}$ above are 5.300, 1.700 and 1.906, respectively.

In conclusion, it should be noted that the function seminf has been found to work quite properly on all simulations conducted. When initialised as described above, seminf yields the optimally corrected $\phi(\omega)$ almost instantaneously for low dimensional problems. Although using seminf to solve the optimisation problem (eqn. 7) may be expected to be less efficient computationally than using the specialised algorithm of [1], seminf is simple to use and, unlike the method in [1], it does not require much interaction with the user.

Acknowledgment: We are grateful to Y. Johansson for typing this manuscript in her usual fast and accurate manner.

16 July 1993
Electronics Letters Online No: 19931307

A. Stoica (*Business Studies Dept. Uppsala University, Uppsala, Sweden*)

R. Moses (*Electrical Eng./ Dept, The Ohio State University, Columbus, OH, USA*)

P. Stoica (*Systems and Control Group, Box 27, Uppsala University, S-751 03 Uppsala, Sweden*)

A. Stoica and P. Stoica: on leave from the Bucharest Polytechnic Institute, Bucharest, Romania

References

1 MOSES, R.L. and LIU, D.: 'Optimal nonnegative definite approximation of estimated moving average covariance sequences', *IEEE Trans. Sig. Process.*, 1991, **39**, (9), pp. 2007–2015

2 FEYH, G., and MULLIS, C.T.: 'Moving average separation'. Proc. Int. Conf. Acoust., Speech, Signal Processing, 1988, pp. 2280–2283

3 JACKSON, L.B.: 'Approximate factorization of unfactorable spectral models'. Proc. Int. Conf. Acoust., Speech, Signal Processing, 1985, pp. 324–326

4 CADZOW, J.A., and SUN, Y.: 'Sequences with positive semidefinite Fourier transforms', *IEEE Trans.*, 1986, **ASSP-34**, (6), pp. 1502–1510

5 STOICA, P., and MOSES, R.L.: 'On the unit circle problem: The Schur-Cohn procedure revisited', *Signal. Process.*, 1992, **26**, pp. 95–118

ULTRA-WIDEBAND SYNTHETIC APERTURE RADAR TARGET DETECTION

Timothy Miller, Lee C. Potter,
Randolph L. Moses
Department of Electrical Engineering,
The Ohio State University,
Columbus, OH 43210

ABSTRACT

In this paper we present algorithms and features for detection of targets from ultra-wideband (UWB) synthetic aperture radar imagery. We have developed and implemnted algorithms related to SAR target detection, including prescreening by CFAR detection and detection clustering, and feature-based discrimination. We present results of CFAR prescreening, and of detection using discrimination features, when applied to UWB SAR imagery collected by ARL at Aberdeen Proving Grounds.

INTRODUCTION

We present algorithms aimed at reliable detection of targets from ultra-wideband synthetic aperture radar imagery. The targets are embedded in clutter ranging from benign clutter, such as grassy fields, to heavy clutter from forested areas. We have developed algorithms for both prescreening and discrimination. These algorithms are compatible with ARL's ATR Evaluation Framework [1], and can be combined and evaluated (*e.g.* with detection ROC curves) with prescreening and discrimination algorithms developed by others. (This paper presents such combined evaluation results — we present ROC curves showing performance of a prescreener developed at ARL in conjunction with two discrimination features developed at Ohio State.)

We present results for both prescreening and discrimination algorithms. The prescreener we use is a two-parameter CFAR statistic combined with clustering operations. In addition, the prescreener generates several features on points of interest, with very little computational overhead, to be used in the discrimination stage. We present two additional discrimination features, which are computed only on points of interest identified by the prescreening algorithm. The two features are based on rotational inertia and range line bipolar templates of responses. We provide some physical motivation for the features, and show performance results when applied to UWB SAR imagery from ARL data collections at Aberdeen Proving Grounds.

CFAR PRESCREENING

Our prescreener is based on a two-parameter constant false alarm rate (CFAR) approach applied to the log-magnitude envelope imagery. A fast, memory-efficient C code for the CFAR/cluster prescreener has been implemented based on the Sandia-Sverdrup STARLOS CFAR module.

The CFAR statistic at pixel (i, j) is given by

$$\frac{I_{ij} - m_{ij}}{\sigma_{ij}} \tag{1}$$

where I_{ij} is the corresponding SAR input image pixel, and m_{ij} and σ_{ij} are the corresponding estimates of the local mean and standard deviation, respectively. The mean and standard deviation are estimated locally on a rectangular annulus of pixels centered on the test pixel, I_{ij}; we choose an 8 m diameter annular guard band.

The clustering routine extracts points of interest (POIs) in the scene by applying a threshold to the CFAR statistic image and grouping closely spaced

*Prepared through collobarative participation in the Advanced Sensors Consortium sponsored by the U.S. Army Research Laboratory under the Federated Laboratory Program, Cooperative Agreement DAAL01-96-0001. The U.S. Government is authorized to reproduce and distribute reprints for Government purposes not-withstanding any copyright notation thereon.

Table 1: CFAR prescreening features

1	centroid (meters, UTM)
2	number of detected points in cluster
3	maximum (dB)
4	mean (dB)
5	standard deviation (dB)
	Covariance Features
6	ellipticity of cluster
7	area of 86.5% Gaussian contour (sq. meters)
8	pose angle (degrees east of north)

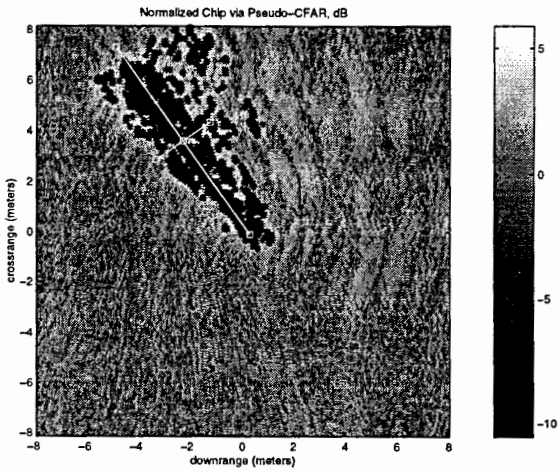

Figure 1: Prescreening feature example target chip, A2R45

detections. The clustering routine scans the range lines of the CFAR image. When a pixel exceeds the threshold, a 5 meter square box centered on that pixel is processed to produce the eight prescreening features in Table 1. CFAR values in the region are zeroed to preclude additional POIs within the box. The clustering approach is chosen to conserve both memory access and computation. Clustering computes a centroid by processing pixels in the 5 m square box; the additional seven prescreen features process the same pixels and require only three additional multiplies per pixel. Thus, the prescresning features are available from the clustering procedure with minimal computational cost.

An illustration of the prescreening features is given in Figure 1. The image is a 16m-by-16m target chip from ARL data collection 2 at Aberdeen Proving Grounds, Run #45 (denoted A2R45). The dark "*" symbols denote CFAR pixels above threshold, and the overlay cross-bars denote the estimated centroid, ellipticity, and pose angle of the target.

A receiver operating characteristic (ROC) plot for ARL Aberdeen data collection #3, Run 60 (A3R60) ($0.37\,km^2$ of data) is shown in Figure 2. A CFAR threshold of 3.1 yields 2054 POIs and a minimum of two detections per vehicle. A quadratic polynomial discriminator (QPD) was trained on all combinations of one, two and three prescreening features. The best single feature performance was observed for the mean CFAR value computed on the 5m-by-5m region. The best QPD combination of three features was maximum CFAR pixel, mean CFAR value, and ellipticity, resulting in 309 detected POIs.

For the A3R60 data set, the combination of three simple prescreening features resulted in 309 POIs ($830/km^2$) for further discrimination processing. CFAR processing provides an invariance to drift in system gain, and can be interpreted as a contrast enhancement step. The CFAR features comprising the best combination of three are computed on the 5m-by-5m box surrounding pixels above threshold and have simple interpretation. First, the maximum CFAR pixel is the classical prescreening statistic identifying points of bright scattering, normalized by the local standard deviation. Second, the mean CFAR value across the 5m-by-5m box characterizes the average strength of radar returns in the immediate vicinity of the peak pixel. The mean CFAR statistic is typically larger for targets than clutter. Third, the ellipticity is computed from the 2-by-2 covariance matrix of CFAR pixels in the 5m-by-5m box. The ellipticity captures the aspect ratio of the cluster of bright pixels. Finally, the centroid of the 5m-by-5m box is reported as the detection location.

DISCRIMINATION FEATURES

In the multi-stage approach, the prescreener is followed by a discriminator, with the purpose of reducing false alarms due to both natural and some man-

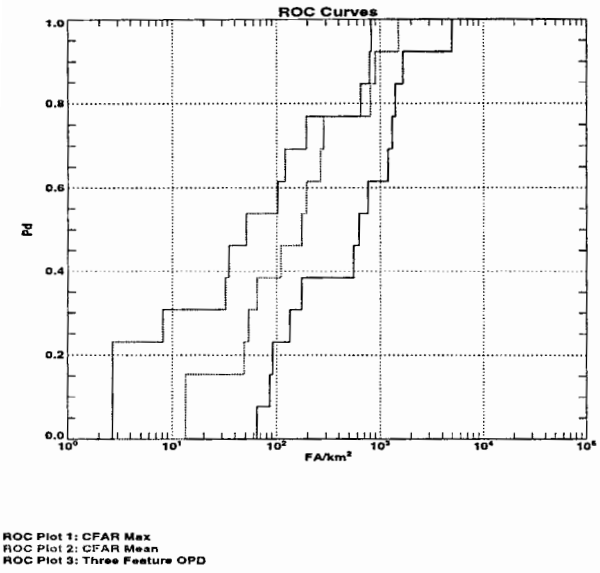

Figure 2: ROC curve for full-band CFAR prescreener, A3R60.

made clutter. Prescreening allows the use of more computationally intensive features at the discrimination stage. We report results for two discrimination features, rotational inertia and a bipolar range line template match.

Rotational inertia

The normalized rotational inertia feature is computed on a binarized image and exploits the size and shape of bright regions in UWB SAR imagery. Applying a user-defined threshold to a 16 m square image chip centered on the POI, bright pixels are morphologically processed by erosions and dilations to produce a bright blob. This is illustrated in Figure 3 for an image chip from A3R60. The rotational inertia, normalized to a circular disk of the same mass, is given by

$$\text{inertia} = \frac{\sum(x_i - \mu_x)^2 + (y_i - \mu_y)^2}{\text{mass}/2\pi} \qquad (2)$$

Thus, inertia is small for round objects and is very large for elongated objects. For horizontal polarization, normalized rotational inertia has shown to be effective at identifying false alarms due to power lines; the feature can be computed from either bipolar or

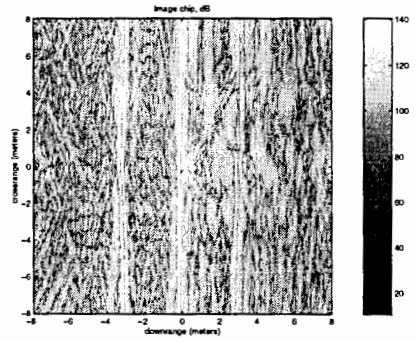

(a) chip 18

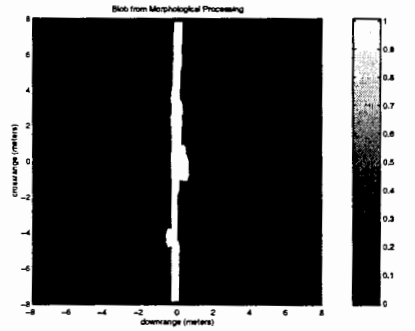

(b) chip 18 binary blob

Figure 3: Blob by morphological filtering for example target chip, A2R45.

log magnitude imagery with similar results. Figure 4 shows the separation of target and power line histograms for A3R60 image chips specified using an ARL prescreener output list of 110 points of interest (POIs).

Bipolar Templates

The bipolar signature feature is computed on a range line extracted from a bipolar image, and seeks to identify differences in the one-dimensional, wideband responses from trees and vehicles. Figures 5 and 6 show selected signatures from POIs in A3R60. From the peak within a 5m square box centered on the POI, we select a range segment extending 0.7m before and 1.0m after the peak (-2.33ns to 3.33ns). The feature is then computed as the correlation of the segment, $s(n)$, with a 1.7m template, $t(n)$, given by $\left(\sum_n s(n)t(n)\right)/\|s\|$. The template is the difference of means from normalized target and tree responses.

Figure 7 shows the templates, *i.e.*, means of normalized signatures (normalized to unit energy and

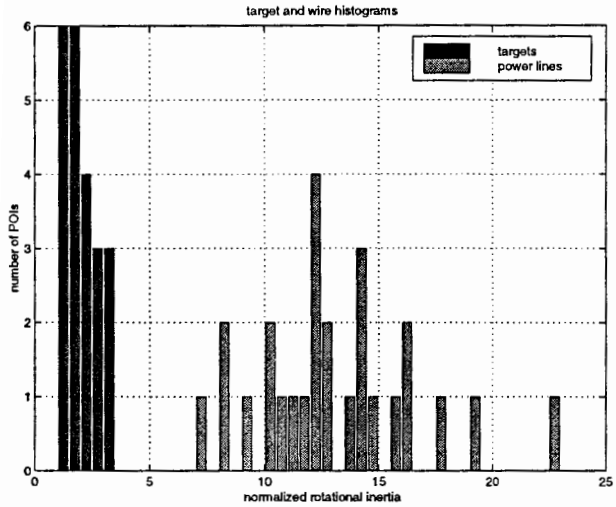

Figure 4: Rotational inertia histograms for power lines and targets, A3R60 horizontal polarization.

positive peak) from trees and targets in A2R45 and A2R60. In Figure 8, the mean target template is compared to ± 1 standard deviation of the normalized tree signatures (dashed lines). Although the means are more distinguishable in A2R45 than A3R60, the target template largely lies within one standard deviation of the tree template. Therefore, an energy measure, such as correlation, will not provide strong discrimination. On the A3R60 data set, the resubstitution method yielded only approximately 55% elimination of false alarms. A covariance weighted template (Fisher discriminant) is not robustly trainable on the A3R60 data set and consequently emphasizes excessively high frequency components.

The similarity of targets and trees may be explained by the dominant role of specular responses in the signature energy. However, the trees in general are more electrically lossy than vehicles; this is evidenced by the slightly wider main lobe for the tree response in Figures 7(a) and 7(b). Identification and exploitation of invariant, observable discriminants remains a continuing goal.

CONCLUSIONS

We have presented algorithms for both prescreening and target discrimination for UWB SAR imagery. The algorithms are compliant with the ARL

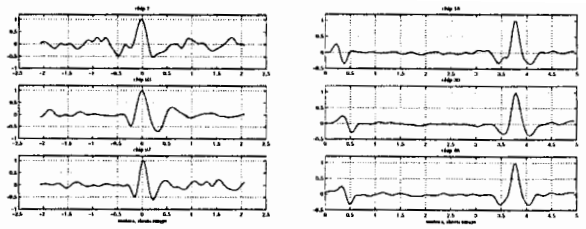

(a) trees (b) power poles

Figure 5: Example normalized bipolar signatures from trees and power poles; segments taken from A3R60 bipolar imagery, horizontal polarization.

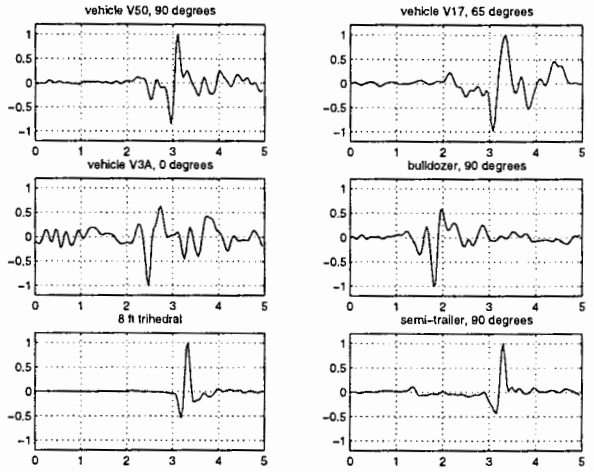

Figure 6: Example normalized bipolar signatures from targets; segments taken from A3R60 bipolar imagery, horizontal polarization.

UWB SAR ATR Evaluation Framework, and this facilitates combining algorithms developed by several researchers. We have presented ROC curves to quantify the effectiveness of the algorithms both for prescreening and for target discrimination on prescreened points of interest.

Current work is focused on improved discrimination feature generation, and on combining these features with other features developed at ARL and by other UWB ATR researchers.

[1] L. Nguyen, R. Kapoor, and J. Sichina, "Detection Algorithms for Ultra-Wideband Foliage Penetration Radar," *Proc. SPIE OE/Aerospace*

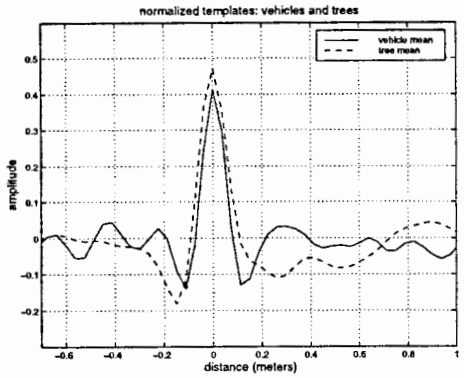

(a) A2R45

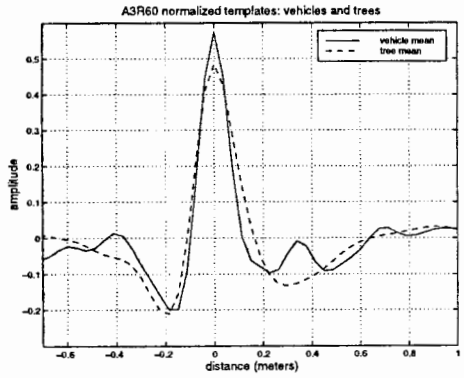

(b) A3R60

Figure 7: Bipolar signature template means for vehicles and trees, taken from two ARL data collections, horizontal polarization

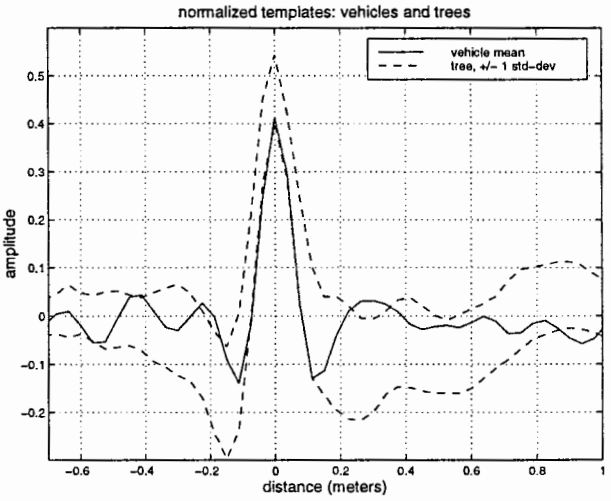

Figure 8: A2R45 vehicle mean bipolar signature template, compared to mean ± 1 stdev of tree template.

Science and Sensing Conference, Orlando, FL (April 1997).

[2] R. Carrière, L. Potter, R. Moses and C. Ying, "Radar Target Modeling: A GTD-Based Approach," in *Proc. SPIE OE/Aerospace Science and Sensing Conference*, vol. 2234, pp. 67–78, Orlando, FL (April 1994).

[3] E. Ertin and L. C. Potter, "Polarimetric classification of scattering centers," submitted to *IEEE Transaction on Aerospace and Electronics Systems*, April 1996.

[4] E. Ertin and L. C. Potter, "Phase Center Corrections for ARL BoomSAR Motion Compensation Files," IPS Laboratory Technical Report TR-97-01, The Ohio State University, March 1997.

[5] M. Gerry, L. Potter, A. van der Merwe and I. Gupta, "A Parametric Model for Synthetic Aperture Radar Measurements," *IEEE Trans Antennas and Propagation*, submitted April 1997.

[6] J. McCorkle and M. Rofheart, "An order $N^2 \log(N)$ backprojection algorithm for focusing wide-angle, wide-bandwidth, arbitrary motion synthetic aperture radar," *Proceedings of the SPIE International Symposium on Radar Sensor Technology*, SPIE Vol. 2747-05, 1996.

[7] T. Miller, J. McCorkle and L. Potter, "RFI Suppression for Ultra-Wideband Radar," *IEEE Trans Aerospace and Electronics Systems*, vol. 33, no. 4, October 1997.